Icarus 281 (2017) 228–239

Contents lists available at ScienceDirect

Icarus

journal homepage: www.elsevier.com/locate/icarus

Geology and mineralogy of the Auki Crater, Tyrrhena Terra, Mars: A possible post impact-induced hydrothermal system

F.G. Carrozzo[a,*], G. Di Achille[b], F. Salese[c], F. Altieri[a], G. Bellucci[a]

[a] Istituto di Astrofisica e Planetologia Spaziali, INAF, Rome, Italy
[b] Osservatorio Astronomico di Teramo, INAF, Teramo, Italy
[c] International Research School of Planetary Sciences, Dipartimento di Ingegneria e Geologia, Università Gabriele D'Annunzio, Pescara, Italy

ARTICLE INFO

Article history:
Available online 7 September 2016

ABSTRACT

A variety of hydrothermal environments have been documented in terrestrial impact structures. Due to both past water interactions and meteoritic bombardment on the surface of Mars, several authors have predicted various scenarios that include the formation of hydrothermal systems. Geological and mineralogical evidence of past hydrothermal activity have only recently been found on Mars. Here, we present a geological and mineralogical study of the Auki Crater using the spectral and visible imagery data acquired by the CRISM (Compact Reconnaissance Imaging Spectrometer for Mars), CTX (Context Camera) and HiRISE (High Resolution Imaging Science Experiment) instruments on board the NASA MRO mission.

The Auki Crater is a complex crater that is ~38 km in diameter located in Tyrrhena Terra (96.8°E and 15.7°S) and shows a correlation between its mineralogy and morphology. The presence of minerals, such as smectite, silica, zeolite, serpentine, carbonate and chlorite, associated with morphological structures, such as mounds, polygonal terrains, fractures and veins, suggests that the Auki Crater may have hosted a post impact-induced hydrothermal system. Although the distribution of hydrated minerals in and around the central uplift and the stratigraphic relationships of some morphological units could also be explained by the excavation and exhumation of carbonate-rich bedrock units as a consequence of crater formation, we favor the hypothesis of impact-induced hydrothermal circulation within fractures and subsequent mineral deposition. The hydrothermal system could have been active for a relatively long period of time after the impact, thus producing a potential transient habitable environment.

1. Introduction

Impact cratering is one of the most important geological processes in transforming planetary surfaces. Although today the collisions between large bodies are rare events, there was a period of time early in the Solar System when all of the celestial bodies were repeatedly impacted. This activity was particularly intense 3.8 Ga during the Late Heavy Bombardment (Wetherill, 1975; Barlow, 1988; Bogard, 1995); most giant basins that we observe on the inner planets date from this period. Early Mars experienced an intense and brief period of meteoritic bombardment during which its surface was reshaped. During the same period, the Martian crust contained large reserves of water (e.g., Clifford, 1993).

The impact cratering process led to the exhumation of material from depth to the surface, and in some cases to the formation of hydrothermal systems in the presence of water, fractures/open porosity in the rock and a heat source (Osinski and Pierazzo, 2013). Impact craters provide unique windows into the subsurface of planetary bodies and allow for the detection of possible occurrences of aqueous alteration processes that took place under the surface.

Hydrothermal systems on Earth are common in a variety of settings, such as mid-ocean ridges, continental rifts and volcanic areas (Edmond et al., 1979; Hedenquist, 1987; Ishibashi and Urabe, 1995). Hydrothermal systems can also occur in impact structures, where the high temperature is due to the large amount of kinetic energy released and deposited into the rocks of the central uplift by the passage of the shock wave (Osinski and Pierazzo, 2013). Additional heat is generated from the rocks of the central uplift due to the increased geothermal gradient (Osinski et al., 2013). For these reasons, the central uplift plays a major role in the alteration mineralogy because that is the region with the highest temperatures. Evidence of hydrothermal systems in impact structures is present in more than 30% of terrestrial craters (Farrow and Watkinson, 1992; Ames et al., 1998; Zurcher and King, 2004; Osinski et al., 2005a). It is well known that impact-generated hydrothermal

* Corresponding author.
E-mail address: giacomo.carrozzo@iaps.inaf.it (F.G. Carrozzo).

http://dx.doi.org/10.1016/j.icarus.2016.09.001
0019-1035/

systems developed in a variety of sizes of craters, from smaller (1.8 km diameter) to larger (200 km diameter) craters (Ames et al., 1998; Hagerty and Newson, 2003; Naumov, 2005; Osinski, 2005b; Osinski et al., 2013; Osinski and Pierazzo, 2013).

Based on these data, it seems plausible that post-impact hydrothermal activity could have occurred on Mars. In particular, these systems could have been very common on early Mars; for instance, the hypervelocity impact that formed the > 5–10 km diameter Noachian complex craters would have been able to generate shock pressures and temperatures capable of melting the target material in the presence of hot water circulating in the upper layers of the crust (Osinski et al., 2005a).

There are two main high temperature locations where impact-generated hydrothermal deposits can form: the melt sheet in the crater cavity and the central uplift (Osinski and Pierazzo, 2013). Melt-rich deposits can also form on crater ejecta and generate shorter-term hydrothermal systems (Sapers et al., 2015) where the alteration of preexisting rocks occurs due to the presence of fractures (Ehlmann et al., 2011; Marzo et al., 2010; Osinski et al., 2013; Schwenzer and Kring, 2013; Tornabene et al., 2013).

The occurrence of minerals forming in a post-impact hydrothermal system on Mars has long been debated (e.g., Newsom, 1980; Allen et al., 1982; Brakenridge et al., 1985).

Alteration minerals are important indicators of the thermochemical environment at the time of their formation (Schwenzer and Reed, 2013). The interaction of water with hot materials forms a hot rock-water circulatory system that can dissolve, transport, and precipitate various mineral species, resulting in characteristic hydrothermal mineral alteration assemblages (Sapers et al., 2012, 2015).

Determining the role of impacts in the origin of hydrated phases is key for deciphering the early climate of Mars (Tornabene et al., 2014). Hydrated phases associated with craters can form from pre-impact, syn-impact, and/or post-impact events (Tornabene et al., 2013). Delineating which spectral signatures are compatible with one of these scenarios is not trivial (Tornabene et al., 2014).

Only recently, some researchers have provided evidence of a post-impact hydrothermal system in the complex Toro and Majuro craters (Marzo et al., 2010; Mangold et al., 2012; Tornabene et al., 2009, 2013; Osinski et al., 2013).

Here we present a detailed spectral and geological analysis of the Auki Crater, located at 96.8°E and 15.7°S in Tyrrhena Terra on Mars, by means of the Compact Reconnaissance Imaging Spectrometer for Mars (CRISM), High Resolution Imaging Science Experiment (HiRISE) and Context Camera (CTX) on board the Mars Reconnaissance Orbiter (MRO). The crater hosts a variety of hydrated minerals and its peculiar geomorphology provides evidence of past water activity. We propose that the geological and mineralogical history of the Auki Crater was mainly characterized by exhumation of buried hydrated materials and possibly by the formation of a post-impact hydrothermal system.

2. Methods

In the present study, we have completed an analysis of the hydrated minerals associated with the geomorphology using the CRISM spectrometer (Murchie et al., 2007) and the HiRISE (McEwen et al., 2007) and CTX (Malin et al., 2007) cameras on board the MRO probe.

CRISM is an imaging spectrometer that acquires hyperspectral images in the 0.4–4.0 μm range with a spatial resolution up to ~18 m/pixel. In this paper, we describe the results obtained from the analysis of the CRISM cube hrl000082e8 with a spatial resolution of 36 m/pixel. The spectra are converted to I/F and corrected by the cosine of the solar incidence angle, and then the atmospheric correction provided by McGuire et al. (2009) is applied. We remove residual vertical striping using the method of Parente et al. (2008). To remove systematic artifacts and to highlight and resolve spectral features, we subtract a neutral component (featureless spectrum) in each spectrum by assuming it is homogeneous throughout each CRISM observation (Carter and Poulet, 2012). For this purpose, we use ratios between the spectra of interest and spectra with a neutral component.

To identify the minerals, we compare the spectral signatures of the ratioed spectra with the spectra of the ASTER (Baldrige et al., 2009), CRISM (Murchie et al., 2007), USGS (Clark et al., 2007) and RELAB spectral libraries.

The choice of the denominator spectrum is fundamental for a correct interpretation of the ratioed spectra. It is selected according to the following criteria:

1. It must be a spectrally neutral component to emphasize the spectral features;
2. It is an average of spectra taken in the same column of the numerator spectra to correct the residual instrument artifacts and reduce detector noise that changes from column to column;
3. It must be taken in the neighborhood of the area of interest to reduce most of the common mineral component.

It is not always possible to satisfy all of the criteria listed above and this must be taken into account in the interpretation of the ratioed spectra. Moreover, this procedure works well if the denominator spectra have a phase similar to that of numerator spectra, but, as we will see, that is not always the case. The ratioed spectra may continue to have multiple phases that contribute to the spectrum with its spectral features (Wiseman et al., 2013). For this reason, when we compare a ratioed spectrum with those from the laboratory, it must be taken into account that more phases may continue to affect the band positions.

For the geological and morphometric analyses, we used high-resolution imagery and topography from ESA Mars Express and NASA MRO (Mars Reconnaissance Orbiter) missions. In particular, HRSC (High Resolution Stereo Camera, Neukum et al., 2004) data (visible nadir image at 12.5 m/pixel and stereo-derived topography at 100 m/pixel) were used for the overall crater context, while CTX (ConTeXt, Malin et al., 2007) and HiRISE (High Resolution Imaging Science Experiment, McEwen et al., 2007) images supported the detailed analysis of the floor and central part of the crater. The latter two datasets were also used to derive high-resolution topography (down to 7 m/pixel from CTX and 1 m/pixel from HiRISE) through the NASA Stereo Pipeline software (Moratto et al., 2010). All of the data were georeferenced and co-registered using the equirectangular projection and the Mars IAU2000 reference ellipsoid. Finally, the imagery, spectral data and topography were imported into the GIS (Geographic Information System, ArcGIS v.10.2.2) environment to obtain a multitemporal/multisensor/multiscale view of the studied crater. We delineated the map units, taking into account their morphology/morphometry, surface properties, texture at different scales (e.g., relative tonal differences from visible imagery, thermal inertia, rough or smooth texture), and their internal sedimentary structure when possible (from erosional windows, crater walls or scarps). The latter approach allowed us to i) identify the main geological/geomorphological units and to ii) correlate the defined units with the mineralogical observations from CRISM (Figs. 1 and 4).

3. Geological and mineralogical observations

In the following paragraphs we describe the geology, geomorphology, spectral units and their relationships within the studied crater.

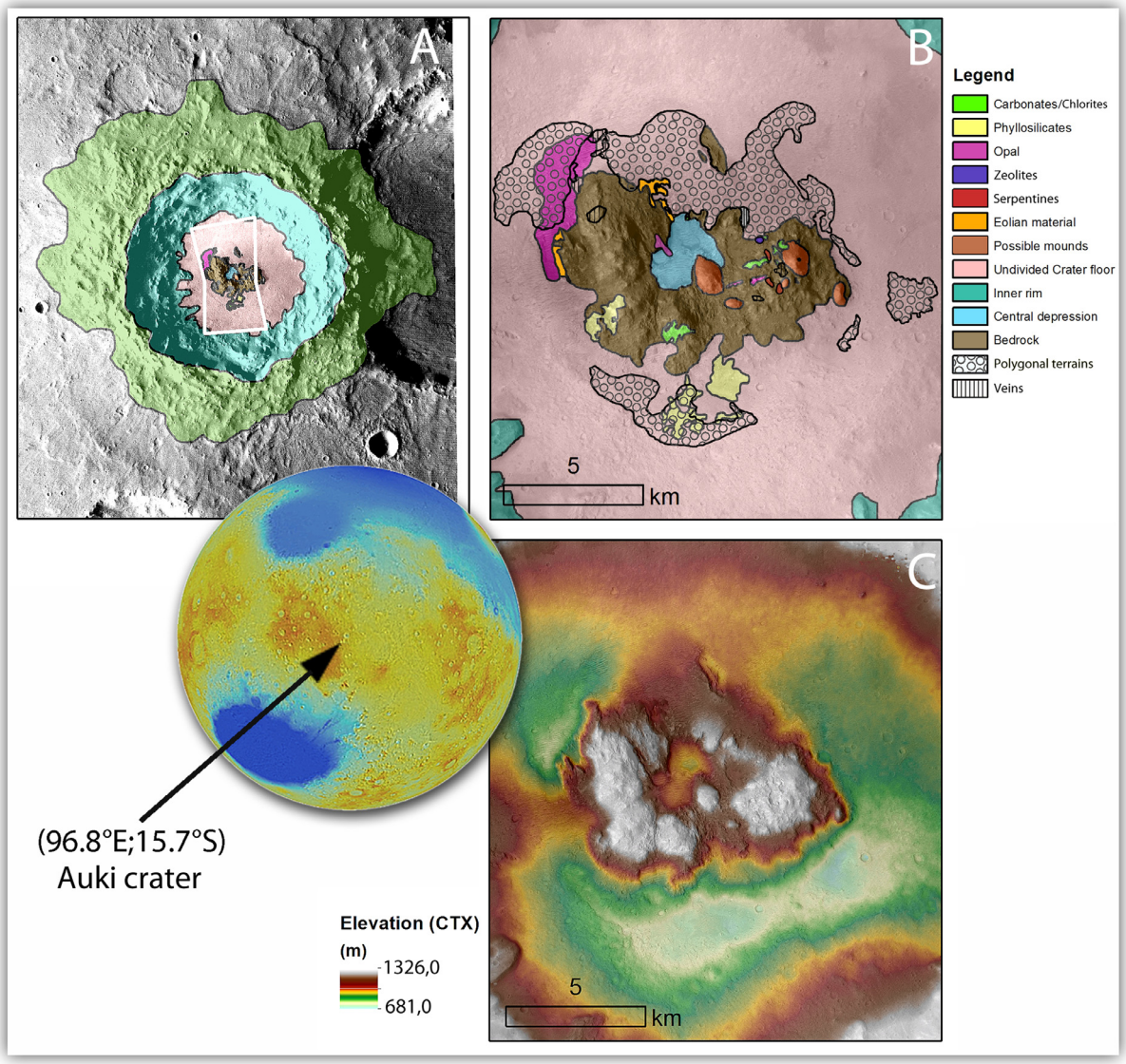

Fig. 1. Location map of the Auki Crater (globe) and overall geomorphologic map of the crater showing (A) the footprint of the CRISM observation; (B) close-up of the geomorphological map for the central peak pit; (C) stereo-derived topography of the same region as figure B.

3.1. Geological context

The Auki Crater is located in the southeastern part of Tyrrhena Terra and is centered at approximately 15.7°S and 96.8°E (Fig. 1). It is a complex crater ~38 km in diameter. The crater ejecta are relatively well preserved and are visible as far as 60 km from the crater center.

The inner crater rim is terraced and is characterized by the presence of several centripetal rotational landslides and collapses emplaced during the modification of the transient cavity generated by the impact. The inner rim slope appears rather unmodified by subsequent erosional processes. In fact, the rim lacks ravines, gullies and any other evidence suggestive of post-impact modifications by hydrological and/or glacial processes, while the crater floor shows few superimposed craters and patches of eolian deposits. The maximum rim to floor depth is approximately 2.2 km based on CTX stereo-derived topographic data; the latter depth is consistent with the latest scaling laws for crater depth obtained from the best-preserved craters on Mars (Tornabene et al., 2013). Except for relatively widespread high albedo TARs (Transverse Aeolian Ridges) and small ergs of dark eolian deposits concentrated around the northern part of the crater center, there are no other significant crater infilling materials.

Located in the center of the crater is a peak with a central depression, likely a remnant of the central uplift formed during the impact.

The crater floor shows an overall rough texture and several small (few hundreds of meters in diameter) impact craters. Based on CTX and HiRISE images, it is possible to identify light-toned regions characterized by the presence of honeycomb and polygonal terrains, especially in association with the deepest regions of the crater floor (Figs. 1 and 2). A polygonal pattern is visible almost everywhere in the portions of the crater floor covered by high-resolution images. Moreover, the polygonal terrains can be divided into three main types based on their morphology and stratigraphy: upper, intermediate, and lower, starting from the highest to the lowest elevation of the polygonal outcrops within the crater floor deposits series (Fig. 2A, B and C, respectively). In particular, the honeycomb polygonal terrains (Fig. 2A) crop out in the highest positions of the crater floor and likely represent the youngest (and

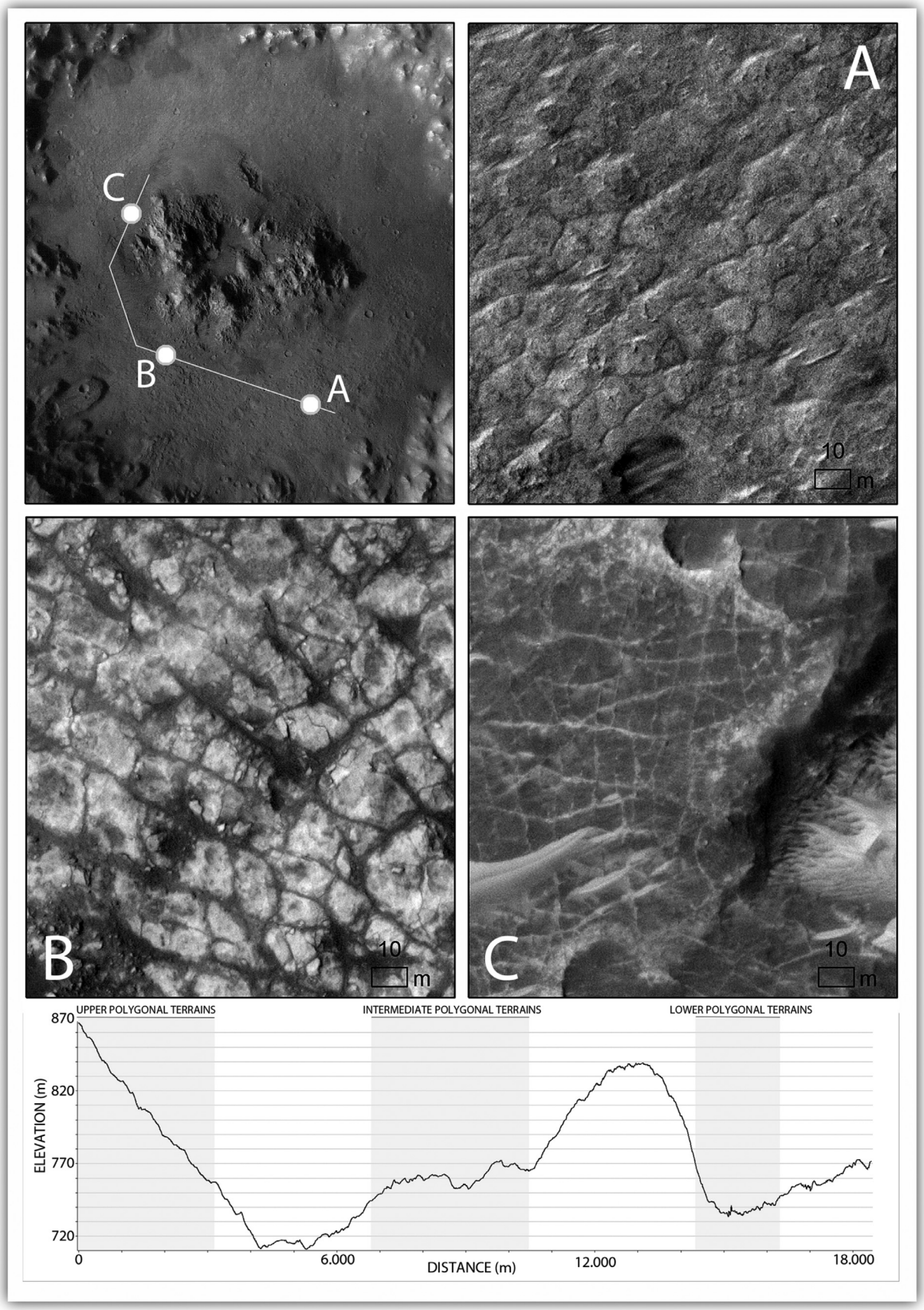

Fig. 2. Close-up view from HiRISE images and location of the polygonal terrains: (A) honeycomb pattern, (B) polygonal cracks and bright concretional layer, (C) inverted veins polygonal network; see text and Fig. 7 for explanations. HiRISE images: ESP_020161_1640 and PSP_005683_1640, ESP_011458_1640. An approximate distribution of the different polygonal terrains it is shown along the topographic profile in the bottom panel. The profile it is extracted from the line of the upper-right panel.

less eroded) deposits of the crater floor sequence. The intermediate polygonal terrains are light-toned in HiRISE grayscale images (Fig. 2B) and are found as raised outlying and irregular patches at intermediate elevations almost everywhere within the portion of the crater floor covered by high-resolution images. Finally, the lower polygonal terrains are visible as rectilinear, light-toned and crosscutting ridges rising above the dark-toned surrounding materials (Fig. 2C). Based on the latter observations, we interpret the above-mentioned outcrops as evidence of three different preservation stages and stratigraphic exposures of the crater floor deposits sequence. Specifically, the upper are interpreted as relatively pristine, the intermediate as eroded/deflated, and the lower terrains as the oldest and topographically inverted.

The crater does not show a typical central peak, although a hilly region (up to more than 200 m high with respect to the surrounding crater floor) is visible in the central floor of the crater (Fig. 1). The latter raised area has a broad annular shape with a central depression and is encircled by a few topographic lows, especially in the southern part of the crater center (Fig. 1). This central uplifted area could be interpreted as a peak pit or summit pit (e.g., Barlow, 2006). The hilly regions of the crater center consist of rocky materials on the western side (Fig. 3A). The latter rocks appear highly fractured by a crosscutting network of NS and EW trending sets of joints. In places the fractures are evidenced by a network of white veins (Fig. 3B). The eastern portion of the peak pit area is a few tens of meters less elevated with respect to the western side and is characterized by the presence of a few small rounded hills that range from a few hundred meters up to 1 km in diameter. The hills have domical structure with smooth and light-toned summits resembling mound features. Finally, joints, fractures, and veins are also visible in the eastern side of the peak pit. However, veins in this region show a darker tone and are larger and apparently more massive with respect to those observed in the western side of the crater peak pit (Fig. 3C).

3.2. Spectral analysis: identified minerals

Using the ratioed spectra we have identified various groups of minerals: phyllosilicates, carbonates, chlorites, hydrated silica, zeolites, olivines and pyroxenes. In the following paragraphs we discuss their absorptions caused by electronic and vibrational transitions occurring in the wavelength range from 1.0 to 2.6 μm. CRISM data reveal a wide variety of spectra in the Auki Crater. Hydrated minerals are present in a variety of geologic settings within the crater. Deposits of hydrated minerals are observed in the central uplift and on the crater floor.

For each class of minerals we provide spectra, spatial distribution and geologic context. In Fig. 4 we show the spatial distribution of the band depth for absorptions at ~1.9, ~2.2, ~2.3 and ~2.5 μm.

3.2.1. Phyllosilicates

Smectites are 2:1 phyllosilicates and they are detected primarily by the absorptions of water near 1.4 and 1.9 μm and by using the position of the metal-OH band from 2.2 to 2.4 μm, where the exact position allows the different types of phyllosilicates to be discerned (Noe Dobrea et al., 2010). A band near 2.2 μm indicates Al-rich phyllosilicates, whereas Fe/Mg-rich phyllosilicates are identified by absorptions from 2.28 to 2.35 μm (Noe Dobrea et al., 2010; Viviano et al., 2013). The latter shifts from 2.28 μm for nontronite to 2.35 μm for corrensite (Loizeau et al., 2007; Mustard et al., 2008). CRISM spectra exhibit a spectral absorption at 2.32 μm (Fig. 5). This absorption is consistent with the presence of Mg-rich clay minerals including vermiculite, hectorite and sepiolite (Ehlmann et al., 2011). These phyllosilicates often occur in association with other phases.

In the spectra we also observe the presence of a strong positive slope from 1.0 μm to 1.5 μm (Fig. 5). This broad absorption could indicate the presence of ferrous (Fe^{2+}) bearing minerals (Mustard et al., 2007). The shape of this absorption can mask the water feature at 1.4 μm that appears less evident in the CRISM spectra with respect to those of other spectral libraries. Possible ferrous components are olivines, pyroxenes and ferrous chlorites (McKeown et al., 2009); these minerals are observed within the crater.

In our study, Mg-smectites (e.g., hectorite, saponite) are uniquely identified by absorption features centered near 1.41, 1.92 and 2.31 μm. We are not able to distinguish between these phases because they have the same minima. Other phyllosilicates, such as talc, can be identified thanks to the same absorptions, but we exclude them because an additional absorption at 2.39 μm is not found. Although the latter band is present in some laboratory spectra of saponite, it cannot be considered diagnostic because it is absent in other spectra.

Serpentine can be distinguished from other minerals thanks to the numerous combination overtones of the metal-OH bending and stretching. The strongest absorption, due to the Mg-OH stretching, is centered at 2.32 μm, while a narrow band due to an OH stretch overtone is at 1.39 μm. In Fe-serpentines, these bands shift at longer wavelengths (Ehlmann et al., 2009). An additional broad shallow absorption at 2.10–2.12 μm and a band centered near 2.51 μm complete the set of absorptions diagnostic of serpentine in the range of wavelengths studied (Ehlmann et al., 2010). In a few locations, the CRISM data have revealed the presence of absorptions near 2.10–2.12 and 2.52–2.53 μm and additional absorptions at 1.40, 1.92 and 2.31 μm (Fig. 5). According to the interpretation of Ehlmann et al. (2009), Mg-serpentine has all the characteristics to be the best candidate. Stoichiometric serpentine would not have molecular water in its structure, but, as for terrestrial serpentine samples, we observe the absorptions at 1.9 μm in the CRISM spectra (Ehlmann et al., 2009). This feature can be caused by intermixed hydrated phases or an imperfect crystalline form (Ehlmann et al., 2010).

Al-smectite montmorillonite could be present in association with hydrated silica (see paragraph 3.2.2), while Fe-smectite nontronite could be present in a mixture with carbonate (see paragraph 3.2.3). Their detection is based on diagnostic absorption features near 2.2 μm and near 2.29 μm, respectively (Mustard et al., 2008).

3.2.2. Hydrated silica

The detection of hydrated silica is based on the position of an OH overtone band at ~1.4 μm, an H_2O overtone band at ~1.9 μm, and a width Si-OH band centered at ~2.2 μm (Mustard et al., 2008).

Hydrated silica can be divided in three categories on the basis of its crystalline phase: the least crystalline is hydrated glass, followed by opal and microcrystalline quartz (Flörke et al., 1991; Smith et al., 2013).

The most diagnostic indicators for detection of silica phases are the positions of the ~1.4 μm and ~2.2 μm features (Rice et al., 2013; Smith et al., 2013). The first band allows for distinction between hydrated glass and other hydrated silica and the second can be used to discern amorphous silica (e.g., opal) from microcrystalline quartz (e.g., chalcedony).

The analyzed CRISM spectra display a clear absorption at 2.21 μm extending from 2.15 to 2.36 μm, and additional features at 1.41 and 1.91 μm (Fig. 5).

We exclude hydrated glass due to the absence of a characteristic band near 1.38 μm (Smith et al., 2013). In fact, in the CRISM data the spectra exhibit a band centered at 1.41 μm. Although some authors (Rice et al., 2013; Smith et al., 2013) use the minimum at 1.4 μm to discern between opaline silica and microcrystalline

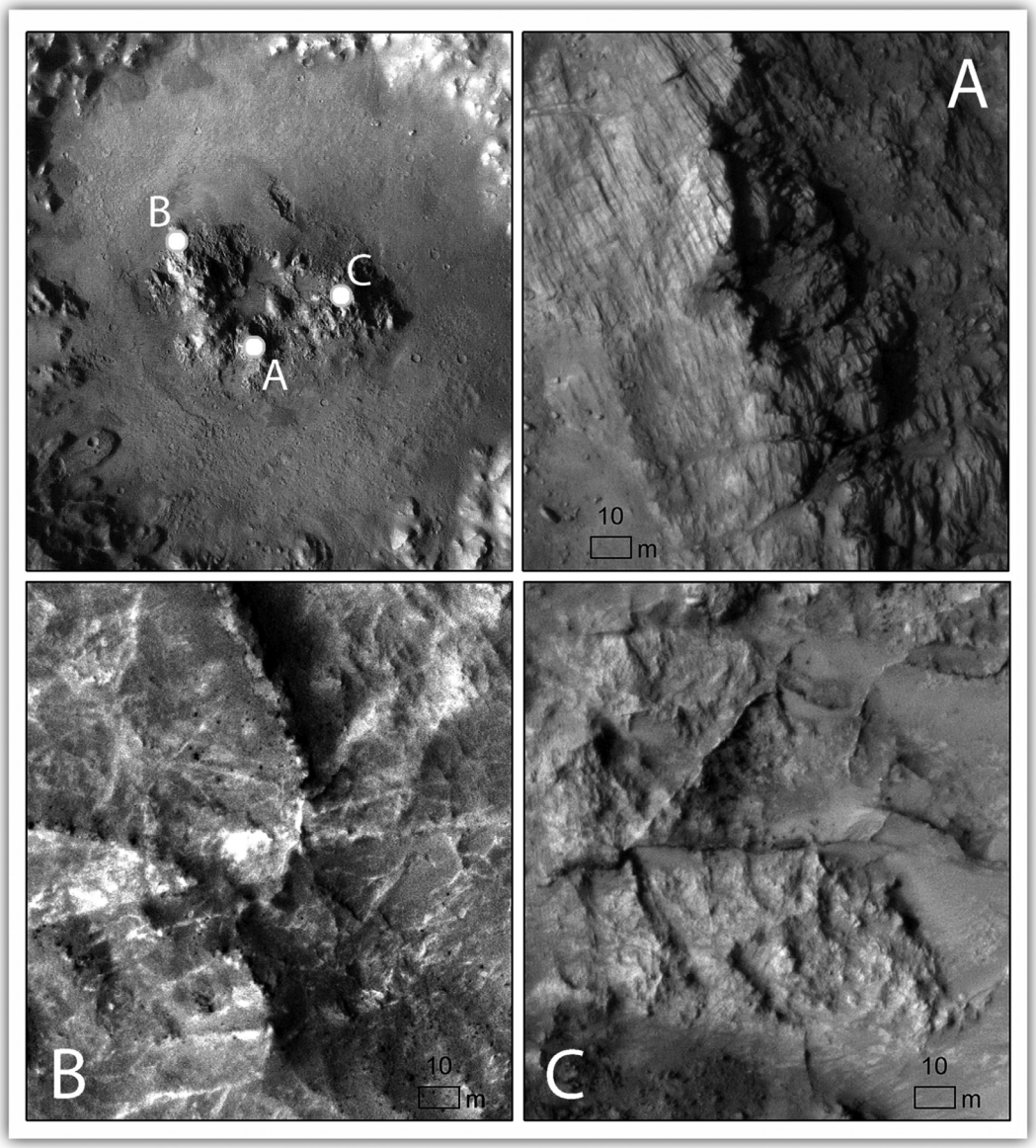

Fig. 3. Close-up view from HiRISE images and location of the joints, fractures and veins visible on the central peak pit units: (A) fractures network on the exhumed bedrock, (B) bright veins, (C) inverted/raised dark veins/ridges. HiRISE images: ESP_020161_1640 and PSP_005683_1640, ESP_011458_1640.

quartz in their sample sets, the observed band position does not allow for distinction between the two type of hydrated silica because it falls into the limit of the wavelength ranges that characterize both phases (Rice et al., 2013; Smith et al., 2013).

On the other hand, the use of the 2.2 µm band is not enough to make a unique interpretation with respect to the different types of opaline silica, opal-A, opal-CT and opal-C (Rice et al., 2013), and at the same time distinguish between three different silica categories. Other studies (Milliken et al., 2008; Smith et al., 2013; Skok et al., 2010) used the position and the symmetry of this band to distinguish the various opaline silicates. Following Rice et al. (2013), we prefer to adopt a conservative approach because in the studies mentioned above, the analyzed spectra are not taken at the same conditions as those observed in a terrestrial laboratory.

In our opinion, on the basis of these considerations, the observed absorption features are consistent with opal and/or chalcedony-cherts.

Although in these CRISM spectra the prominent phase should be the hydrated silica, a mixture with Al-rich phyllosilicate is possible because the 2.2 µm band is sharper than that of a pure silica phase. Similar spectra have been observed by other authors (Bishop et al., 2008; Mangold et al., 2012). For example, in phyllosilicates the Al-OH band near ~2.2 µm is narrow, while in hydrated silica the same absorption is clearly wider due to the overlapping of Si-OH at 2.21 µm and of H-bound Si-OH at 2.26 µm (Milliken et al., 2008; Pan and Ehlmann, 2013). The best spectral match is a mixture of opal with montmorillonite. Kaolinite could be another candidate, but we exclude it due to the absence of a doublet at 2.16 and 2.21 µm.

3.2.3. Carbonates

Carbonates are identified by paired bands located near 2.3–2.35 and 2.5–2.55 µm (Michalski and Niles, 2010). The CRISM spectra exhibit absorptions near 2.32 and 2.53 µm. In Fig. 5, we use BD-CARBO spectral index of Pelkey et al. (2007) to map the occurrence of both bands (Fig. 4). The occurrence of features near 1.4 µm and a deeper band near 1.9 µm could imply a mixture with hydrated phases, probably phyllosilicates. These two bands do not show con-

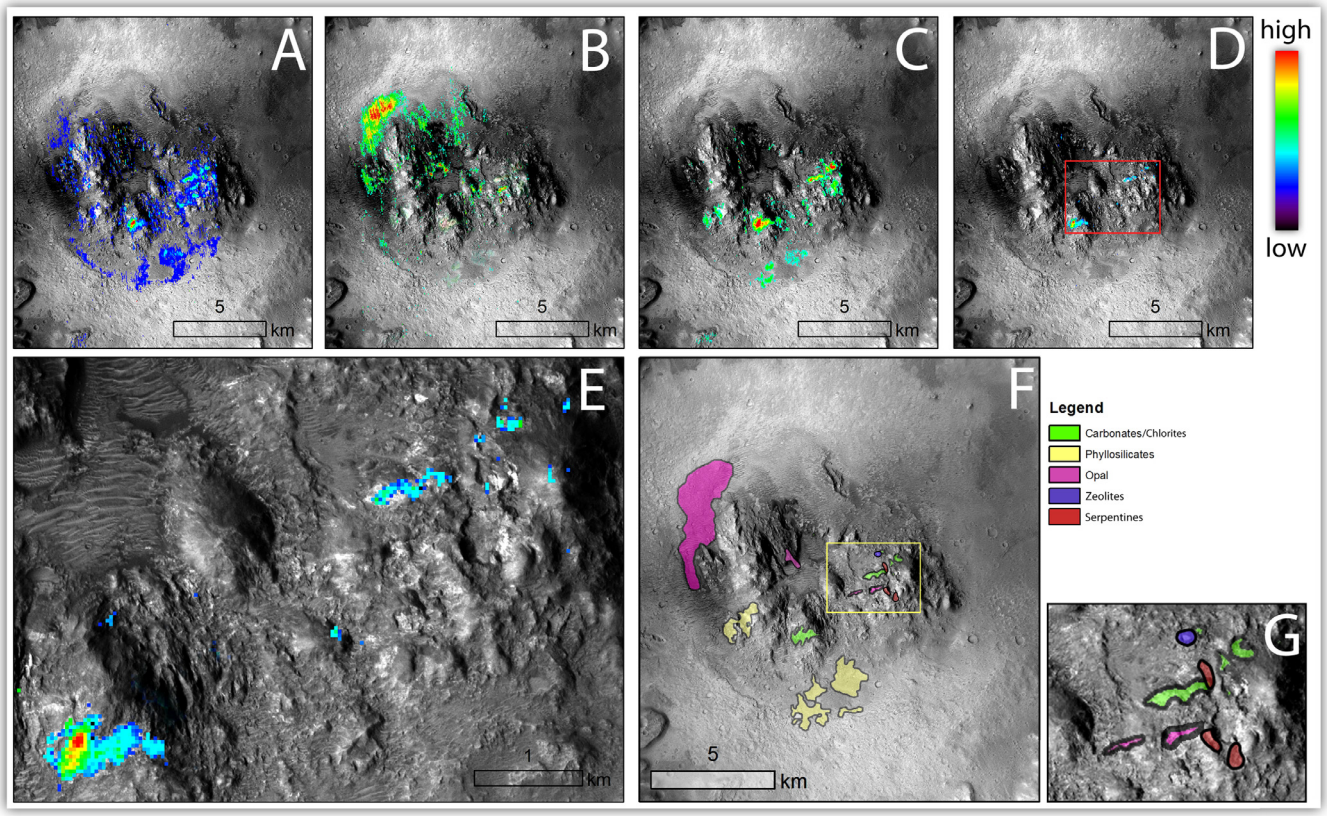

Fig. 4. Spatial distribution of the band depth at (A) 1.9 µm used for identification of hydrated minerals (note that the NE-SW distribution of the minerals likely reflects the fracture pattern), (B) 2.2 µm for identification of silica, (C) 2.3 µm for identification of carbonates, phyllosilicates and chlorites, and (D) BDCARBO for identification of carbonates. The value ranges are 0.005–0.040, 0.007–0.020, 0.007–0.030 and 0.02–0.07, respectively. In panel (E) is a close-up view (see red area in the d panel for location) of the peak pit. Panel (F) shows the distribution of the most representative minerals and (G) shows a close-up of the central peak pit of panel F (see also Fig. 1). (For interpretation of the references to colour in this figure legend, the reader is referred to the web version of this article.)

siderable variation in position, varying between 1.41–1.42 µm and 1.91–1.92 µm, thus reducing the choice to a few minerals. A mixture with smectites could explain the bands due to hydration and the shift of the 2.3 µm band to lower wavelengths.

The positions of the bands may be consistent with the presence of carbonates (e.g., magnesite, calcite) with a mixture of Mg-phyllosilicates (e.g., vermiculite, saponite). These types of spectra are observed in many areas on Mars, such as Nili Fossae, Libya Mons and Jezero crater (Brown et al., 2010; Bishop et al., 2010; Goudge et al., 2015). Sometimes the spectra of carbonates exhibit a weak feature or shoulder at 2.24 µm, suggesting that they are present in association with another component, providing the best match with chlorite. Nontronite cannot be excluded because this absorption is often present in the library spectra of this mineral.

Other hydrated phases cannot be ruled out, but in a mixture of carbonate and phyllosilicate, some complex considerations should be taken into account. In Al-smectite, the metal-OH absorption falls at approximately 2.2 µm, whereas the substitution of metals in the cation can shift the band approximately 2.3 µm. With increasing proportions of Mg to Fe, the band shifts to longer wavelengths (Bishop et al., 2002). Specifically, Fe-OH absorption features have a band near 2.28 µm, whereas the Mg-OH band falls in the 2.32–2.34 µm range (Clark et al., 1990; Loizeau et al., 2007). For example, the band center of montmorillonite (Al-smectite) is near 2.20–2.21 µm, of nontronite (Fe-smectite) is near 2.29 µm, and of sepiolite, saponite and hectorite (Mg-smectites) is near 2.31–2.32 µm, whereas that of chlinochlore (Fe-chlorite) is near 2.33–2.34 µm (Ehlmann et al., 2009).

The band centers in carbonates are variable with the dominant cation in the same way. A shift to longer wavelength is observed on passing from Mg to Fe/Ca content. Mg-carbonates have band minima near 2.30 and 2.50 µm, while Fe/Ca-carbonates have minima near 2.33 and 2.53 µm (Brown et al., 2010).

For this reason, it is possible that the band centered at 2.32 µm is an average between multiple phases, such as Fe-smectite+Fe/Ca-carbonate or Mg-smectite+Mg-carbonate or Fe-chlorite+Mg-carbonate. It is important also to emphasize that a mineral mixture can exhibit nonlinear trends of the mineral abundances and that this is especially problematic if fine-grained materials are present (Bishop et al., 2013). For example, a study of Fe-smectite+Mg-carbonate mixtures has shown that the resulting position of the 2.3 µm band is strongly influenced by the nontronite. Small amounts of smectite shift the band center toward that of Fe-smectite (e.g., nontronite) (Bishop et al., 2013). On the basis of these considerations, a mixture between nontronite+calcite (Fe-smectite, band center near 2.29 µm, and Ca-carbonate, band center near 2.34 µm, respectively) or between chlorite+magnesite (Fe/Mg-clay, band center at 2.34 µm, and Mg-carbonate, band center at 2.30 µm, respectively) is possible, and could result in a shift of the band in an intermediate position, such as that observed at 2.32 µm.

However, the spectra of the carbonates mentioned above do not fit CRISM data around the 1 µm band, where a broad absorption appears (Fig. 5) consistent with a strong Fe^{2+} content. The positive slope in the 1.1–1.8 µm range is typical of Fe-carbonate (Wray et al., 2011). Potential carbonate candidates are ankerite and siderite with a band in the range 2.33–2.35 µm and 2.53–2.54 µm and a broad absorption in the 1.0–1.5 µm range. Alternatively, a

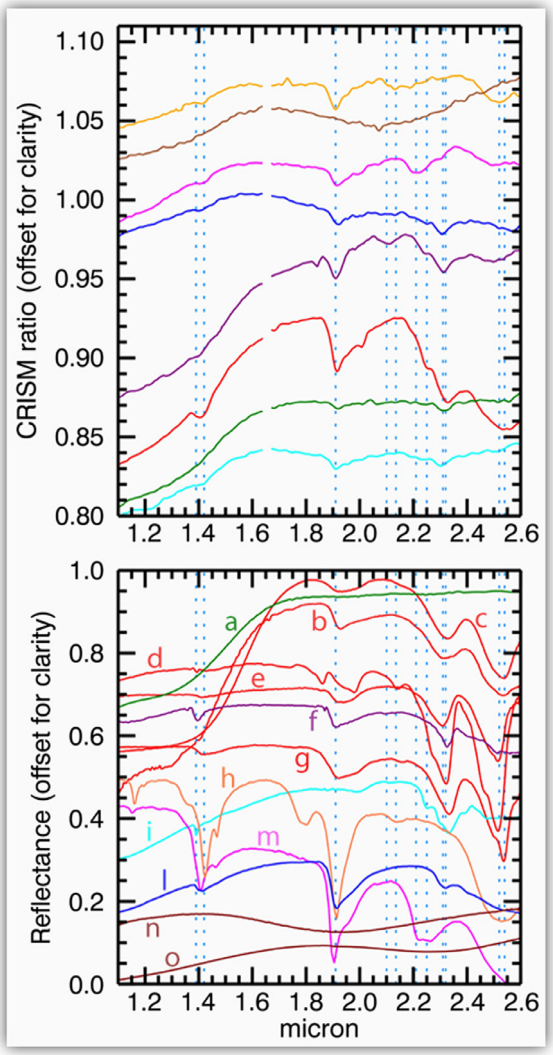

Fig. 5. CRISM spectra ratio (top panel) compared to various library spectra (bottom panel). Olivine is in green color (a-olivine), carbonate in red (b-siderite, c-ankerite, d-calcite, e-calcite, g-dolomite), serpentine in purple (f-serpentine), zeolites in orange (h-analcime), chlorites in cyan (i-chlorite), smectite in blue (l-saponite), silica in magenta (m-opal), pyroxene in maroon (n-LCP, o-HCP). (For interpretation of the references to colour in this figure legend, the reader is referred to the web version of this article.)

mixture containing olivine or oxide could display a broad absorption near 1.0 µm (Ehlmann et al., 2008). We favor the idea that the carbonate-bearing spectra are a mixture of Fe-smectite, olivine and Ca-carbonate. All exposures of carbonates occur in the central uplift and are not present on the crater floor.

The additional analysis of the spectral range above 3 µm could help in the understanding of the composition of the rocks in the uplifts, but the higher noise in these wavelengths makes study of this spectral region difficult.

3.2.4. Other phases

Zeolites are silicates with a combination of absorptions in the 1.0–2.6 µm range (Brown et al., 2010; Ehlmann et al. 2011). In the CRISM spectra we observe strong spectral features at 1.40, 1.91, 2.13 and 2.52 µm (Fig. 5). The bands at 1.12 and 1.79 µm are not observed. As suggested by Ehlmann et al. (2009), these two absorptions could disappear because of the presence of Fe-related minerals hiding the shorter wavelength features. The positions and the shape of these minima indicate that zeolites are present in the form of analcime. We exclude other zeolites, such as mordenite, because in this mineral, the band at 2.53 µm is absent.

A strong absorption is present in chlorite from 2.33 to 2.36 µm, depending on the cation metal-OH (Noe Dobrea et al., 2010). The band moves to longer wavelengths as the Fe content relative to Mg increases (Noe Dobrea et al., 2010). An additional shoulder at 2.25–2.26 µm is observed and results from AlMg-OH or $AlFe^{3+}$-OH stretching modes (Ehlmann et al., 2009). In CRISM spectra the bands do not line up uniquely with any one specific chlorite, probably because it may be mixed with other components. Hence, chlorite could be responsible for the features observed in some spectra, for example, those of carbonate and smectite. In the latter we observe a shoulder at 2.25 µm, a strong absorption at 2.32–2.33 µm and other spectral features near 1.41 and 1.91 µm.

The spectral analysis also revealed mafic and ultramafic materials (e.g., pyroxene and olivine) in the floor and in the uplift of the crater.

The detection of pyroxenes is based on the presence of two broad absorptions, typically at ~1 and ~2 µm. These band centers shift towards longer wavelengths with increasing calcium concentration (Adams, 1974). For this reason, it is possible to make a spectroscopic distinction between low Ca-content (LCP) and high Ca-content (HCP) pyroxenes (Schade et al., 2004). In particular, the band center of LCP is situated near 0.9 and 1.9 µm with a maximum near 1.3 µm, while the band center of HCP is located near 1.05 and 2.3 µm with a reflectance maximum near 1.6 µm (Cloutis and Gaffey, 1991). As the CRISM spectra show absorptions approximately 1.0 µm and in the 2.0–2.2 µm wavelengths range with a maximum near 1.5 µm (Fig. 5), we believe that the spectra in the Auki Crater indicate a mixture of both pyroxenes.

Olivine has a complex absorption approximately 1 µm. It moves toward longer wavelengths with an increasing amount of Fe^{2+} (Sunshine et al., 2004). The right wing of the absorption shifts towards longer wavelengths as the FeO content in the olivine increases (Poulet et al., 2007). However, this may be caused by an increase in the grain size that broadens the bottom of the band so that a forsterite olivine spectrum with very large grains and a fayalite olivine spectrum with smaller grains have similar spectral features (Poulet et al., 2007). The identification of olivine from the CRISM spectra is made thanks to the increase of reflectance in the 1.0–1.7 µm wavelength range (Carrozzo et al., 2012), which results from the overlapping absorptions centered at ~1 µm (Fig. 5).

The positive slope in the 1.0–1.8 µm range is observed in many other spectra and is mentioned in the previous paragraphs. In accordance with other authors (e.g., Bishop et al., 2008; McKeown et al., 2009), we interpreted these spectra to be the result of a mixture of hydrated minerals with pyroxenes and/or olivines, indicating the presence of a ferrous phase (Fe^{2+}).

3.3. Relationships between observed minerals and geology/geomorphology

Based on the observations presented in the previous paragraphs, it can be seen that the hydrated minerals are mostly concentrated within the raised terrains of the central peak pit area and within the surrounding topographic lows located on the southern and northwestern borders of the central hilly regions (Figs. 1 and 4). In particular, by comparing Figs. 1 and 4, it is evident that phyllosilicates are present within the central peak units, visible as scattered patches throughout the whole hilly central region, and also in association with the occurrences of silica and carbonates. Moreover, phyllosilicates seem to be correlated with the two deepest topographic lows along the southern hills of the central peak area; the latter depressions are excavated within the crater floor

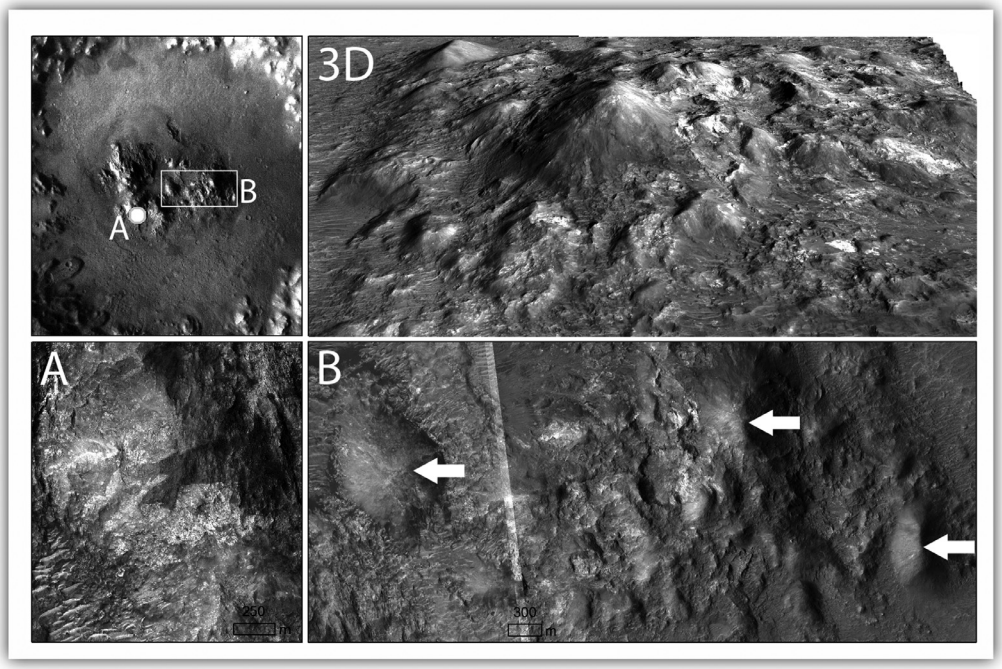

Fig. 6. Close-up view from HiRISE images and (A) location of the bright carbonates outcrop; (B) possible spring mounds (marked by arrows) in the eastern portion of the central peak pit shown also in perspective view (realized from HiRISE stereo-derived topography) in the upper right panel.

units characterized by the occurrence of polygonal terrains (especially the eroded/deflated type, Figs. 1 and 4).

Outcrops with the presence of carbonates are almost exclusively located in the hilly peak pit area (Figs. 1 and 4). The carbonate-bearing rocks have sharp boundaries and are visible as isolated patches surrounded by the layered and fractured rocks of the central peak in the western side of the peak ring (Fig. 4). Whereas, in the eastern side, the carbonate units crop out as a mostly E-W linear oriented patch and at the base of one of the mound-like rounded hills (Figs. 4 and 6).

Finally, silica-rich units are observable within the topographic low in the northwestern portion of the crater floor adjacent to the central hilly region and are associated with the carbonates that outcrop in the eastern peak ring area. The silica-bearing units show the highest concentration of light-toned veins.

4. Discussion and conclusions

We interpret the geology, spectral characteristics and overall evolution of the Auki Crater as follows:

Phyllosilicates are the dominant phase and sometimes occur mixed with other phases. They have been detected in many locations of the central uplift, around its base and in other sites in association with hydrated silica and anhydrous minerals (Fig. 1). Hydrated silica is observed in two units: in the central uplift and in a large area of the floor located in the northwest (Fig. 1). The high-resolution images of the latter area show a network of cross-cutting rectilinear fractures (Fig. 2C). These features appear to be consistent with possible deformation bands observed in Toro crater and described in Marzo et al. (2010). These light-toned structural discontinuities have been suggested to form by extrusion of gas/water-sediment mixtures from the sub-surface, which act as local conduits for vertical flow of fluids in the sub-surface (Marzo et al., 2010).

The distribution of the hydrated minerals in and around the central uplift and the stratigraphic relationships of the carbonate units suggest two main (likely partially overlapping) mechanisms to explain their origin: one is related to the crater formation and subsequent excavation and exhumation of carbonate-rich bedrock units, and the second is connected to impact-induced hydrothermal circulation within fractures and subsequent mineral deposition. The first hypothesis is supported by the fact that the western carbonate outcrops have sharp geometric contacts with the surrounding bedrock, as if it was an entrained megablock of brecciated carbonate-rich material within the crater floor deposits. If this were the case, these latter contacts could be explained by the exhumation/uplift of deeper carbonate-bearing bedrock units during the crater formation.

Although we believe that the latter hypothesis is the most reasonable for the western carbonate outcrop, the hydrothermal hypothesis for the origin of the observed carbonates, and especially for those located in the eastern side of the peak ring area, cannot be ruled out. In fact, in this portion of the central hilly region the carbonates are associated with silica and phyllosilicate occurrences and crop out as an NE-SW elongated patch (likely following a fracture) aligned with a second patch at the base of the possible mound-like features. Although there is no evidence for the depressions at the top of these latter structures to be interpreted as possible vents, the lack of depressions on the observed mounds may be explained through post-depositional erosion and/or concealment by dust deposition (Pondrelli et al., 2011).

Moreover, in this area dark tone veins are present and this observation could further support the hydrothermal circulation hypothesis.

Polygonal terrains, veins and mineral assemblages are interpreted to be the results of diagenetic processes (Fig. 7) involving the formation of desiccation cracks (e.g., El Maary et al., 2010, 2012, 2014), hydrothermal water circulation, and mineral deposition occurring from the ground level to the subsurface phreatic groundwater zone (e.g., Siebach and Grotzinger, 2014). In addition to the straightforward morphological evidence and the topographic locations (erosional windows) of the polygonal terrains, this hypothesis is supported by the fact that the latter terrains are correlated with the spectral evidence for hydrated minerals, such as

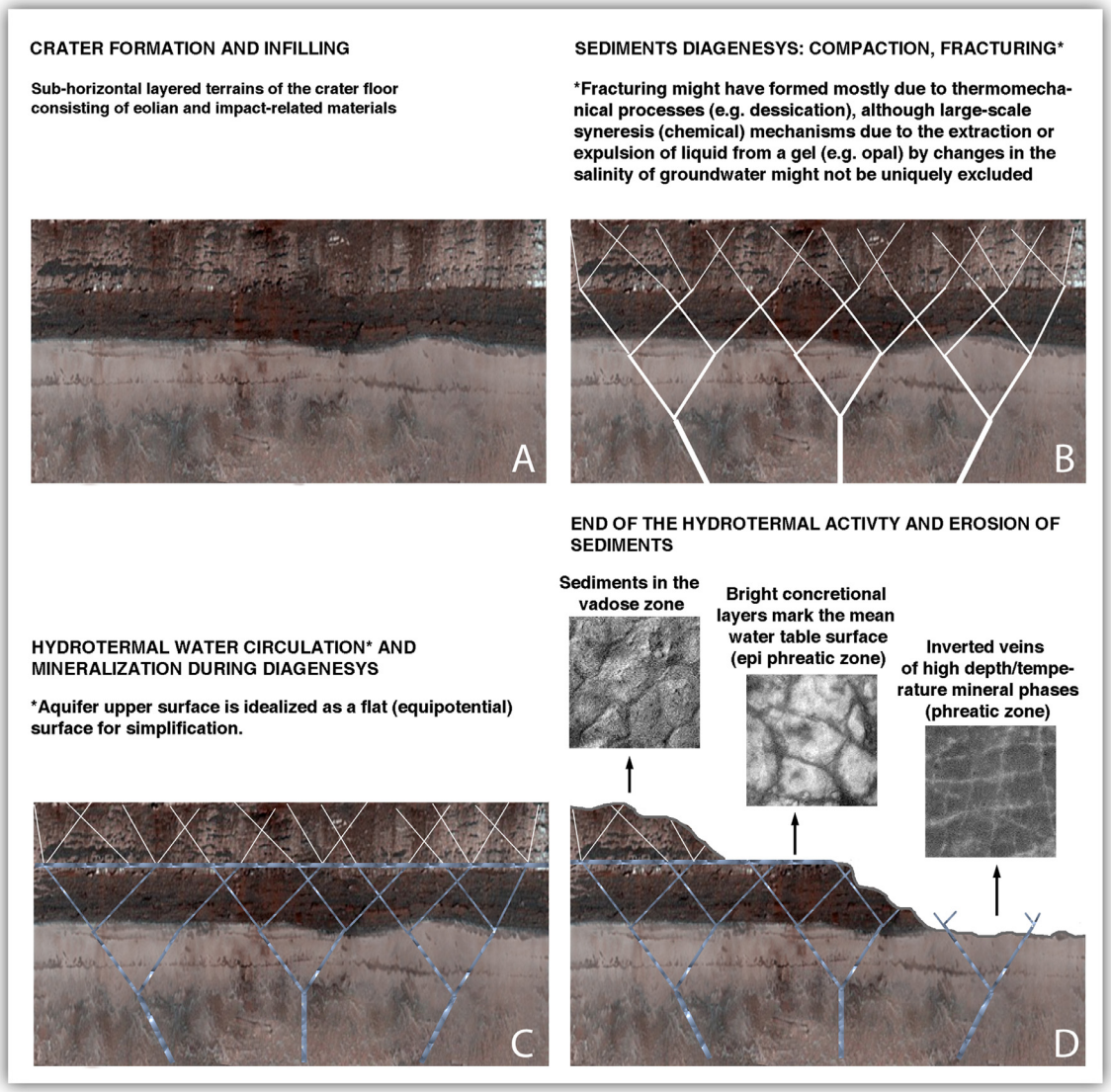

Fig. 7. Schematic cross section representation and synthesis of processes sequence leading to the formation of the polygonal terrains characterizing the crater floor (see Figs. 1 and 2). The layers are for illustration purposes only and do not reflect the scale and the different composition of the actual stratigraphy.

phyllosilicates and silica. The overall spatial distribution of the desiccation cracks and their three main preservation stages from the highest to the lowest crater floor deposits sequence suggest that they likely cover the entire crater floor and are visible only after erosion/deflation and in topographic windows to the deepest layers. In agreement with Brown et al. (2010), our opinion is that the stratigraphic relationship between different mineral units is the result of different temperatures regimes within the zone of hydrothermal alteration. The fact that the deepest inverted type show veins and are correlated with spectral evidence for silica, while the intermediate and highest terrains are not affected by veins and are correlated with spectral signatures for phyllosilicates, might be explained by the vertical zonation of the hydrothermal processes. On Earth, when hydrothermal activity occurs, typical alteration minerals are carbonates, smectites, chlorites, serpentine and zeolites (Naumov, 2005; Ehlamnn et al., 2011; Osinski et al., 2013; Schwenzer and Kring, 2013). In CRISM spectra we observe the same minerals by recognition of diagnostic features in the range of 1.0–2.6 μm. They often occur as a mixture. This suite of minerals is consistent with the development of a post-impact hydrothermal system inside the crater cavity. The duration of the hydrothermal system depends on various factors, such as the impact energy, water availability, and rock permeability (Naumov, 2005; Pierazzo et al., 2005; Loizeau et al., 2012). After the impact, it may have existed for a long period of time. Numerical simulations in a 30 km diameter crater show that it can remain active for approximately 70,000 years (Abramov and Kring, 2005).

Although these minerals form over a wide range of temperature, their association with veins and polygonal terrains suggest that the alteration is due to hydrothermal circulation of fluids. Available data are not sufficient to describe the reaction series and the exact temperatures that generated the observed minerals. However, the presence of hydrated minerals near the olivine-rich units (sometimes olivine-rich units exhibit absorptions due to carbonates) may indicate alteration of the olivine. In other regions of Mars such as Nili Fossae, various authors (Ehlmann et al. 2010; Viviano et al., 2013; Brown et al., 2010) have hypothesized that carbonates might have been a weathering product of olivine, and other authors (Neubeck et al., 2014) have experimentally demonstrated that olivine hydrolysis in a carbonate-rich solution produces serpentine, carbonates and amorphous Si-rich phases in a hydrothermal system, even at low temperatures.

The system was supported by underground water, and given the lack of evidence for surface water runoff, does not necessary imply the occurrence of paleoclimatic conditions favorable for the presence of liquid water at surface. However, the presence of these minerals is indicative of an intermediate to low water/rock ratio (Schwenzer and Kring, 2013).

In summary, the geological evolution of the studied area could be reconstructed with the crater formation, which exhumed/uplifted carbonate-rich bedrock that is visible in the crater peak pit area and activated a vertically zoned hydrothermal system. The latter system determined the alteration of mafic rocks to silica, phyllosilicates, zeolites and chlorites and likely secondary carbonate mineral phases. This scenario is in agreement with that described by Loizeau et al. (2012), where a hydrothermal system is proposed to explain the presence of the same minerals within some craters of Thyrrena Terra.

Finally, given the lack of any signs of hydrological activity from the inner crater rim slope such as valley networks, it can be concluded that the water for the hydrothermal system was provided by underground circulation and/or melting of water ice.

If the hydrothermal activity occurred, it was not restricted to the central uplift but was also present in the crater cavity. Clear evidence of hydrothermal activity on Mars is scarce (Tornabene et al., 2009; Marzo et al., 2010; Mangold et al. 2012; Skok et al., 2012; Osinski et al., 2013). The strong correlation between the observed minerals (carbonate, opaline, smectite, chlorite, serpentine and zeolite) and morphology (veins, polygonal terrains and mounds) of hydrothermal origin makes the studied crater one of the best candidates for hosting an ancient post-impact hydrothermal system.

If life once existed on Mars, it could have been confined to some protective niches, such as that of a post-impact hydrothermal system where liquid water is available and the mineral reactions release elements that can serve as nutrients. A hydrothermal system could produce transient habitable environments and this crater could be a particular target of interest for a future landing site to search for evidence of past life.

Acknowledgements

This work was supported by ASI, Agenzia Spaziale Italiana, and the Italian Ministry of University and Research through the ASI grant no. I/06/08/0 and FIRB grant no. RBFR130ICQ. We thank Giuseppe Marzo for his useful suggestions that improved the data analysis.

References

Abramov, O., Kring, D.A., 2005. Impact-induced hydrothermal activity on early Mars. J. Geophys. Res. 110 (E12S09). doi:10.1029/2005JE002453.
Adams, J.B., 1974. Visible and near-infrared diffuse reflectance spectra of pyroxenes as applied to remote sensing of solid objects in the solar system. J. Geophys. Res. 79 (32), 4829–4836.
Allen, C.C., et al., 1982. Hydrothermally altered impact melt rock and breccia – contributions to the soil of Mars. J. Geophys. Res. 87, 10083–10101.
Ames, D.E., et al., 1998. Dating of a regional hydrothermal system induced by the 1850 Ma Sudbury impact event. Geology 26, 447–450.
Baldridge, A.M., et al., 2009. The ASTER spectral library version 2.0. Remote Sens. Environ. 113, 711–715.
Barlow, N.G., 1988. Crater size-frequency distributions and a revised Martian relative chronology. Icarus 75 (2), 285–305.
Barlow, N.G., 2006. Impact craters in the northern hemisphere of Mars: layered ejecta and central pit characteristics. Meteorit. Planet Sci. 41 (10), 1425–1436.
Bishop, J.L., et al., 2002. The influence of structural Fe, Al and Mg on the infrared OH bands in spectra of dioctahedral smectites. Clay Miner. 37, 607–616.
Bishop, J.L., et al., 2008. Phyllosilicate diversity and past aqueous activity revealed at Mawrth Vallis. Mars Sci. 321, 830–833.
Bishop, J.L., et al., 2010. Mineralogy of Libya Montes and the Southern Isidis Planitia region: CRISM detection of clay, carbonate, olivine and pyroxene, and correlation with HiRISE imagery. In: 41th LPSC. #2147.
Bishop, J.L., et al., 2013. Spectral properties of Ca-,Mg- and Fe-bearing carbonates. In: 44th LPSC. #1719.
Bogard, D.D., 1995. Impact ages of meteorites. Meteoritics 30, 244–268.
Brackenridge, G.R., et al., 1985. Ancient hot springs on Mars: origins and paleo environmental significance of small Martian valleys. Geology 13, 859–862.
Brown, A.J., et al., 2010. Hydrothermal formation of clay-carbonate alteration assemblages in the Nili Fossae region of Mars. Earth Planet. Sci. Lett. 297, 174–182.
Carrozzo, F.G., et al., 2012. Iron mineralogy of the surface of Mars from the 1 μm band spectral properties. J. Geophys. Res. 117 (E00J17). doi:10.1029/2012JE004091.
Carter, J., Poulet, F., 2012. Orbital identification of clays and carbonates in Gusev crater. Icarus 219, 250–253.
Clark, R.N., et al., 1990. High spectral resolution reflectance spectroscopy of minerals. J. Geophys. Res. 95, 12653–12680.
Clark, R.N., et al. (2007). USGS digital spectral library splib06a: U.S. geological survey, Digital Data Series 231.
Clifford, S.M., 1993. A model for the hydrologic and climatic behavior of water on Mars. J. Geophys. Res. 98 (E6) 10.973-11.016.
Cloutis, E.A., Gaffey, M.J., 1991. Pyroxene spectroscopy revisited: spectral-compositional correlations and relationship to geothermometry. J. Geophys. Res. 96 (22), 809–822 826.
Edmond, J.M., et al., 1979. Ridge crest hydrothermal activity and the balances of the major and minor elements in the ocean: the Galapagos data. Earth Planet. Sci. Lett. 46.1, 1–18.
Ehlmann, B.L., et al., 2008. Orbital identification of carbonate-bearing rocks on Mars. Science 322, 1828–1832.
Ehlmann, B.L., et al., 2009. Identification of hydrated silicate minerals on Mars using MRO-CRISM: geologic context near Nili fossae and implications for aqueous alteration. J. Geophys. Res. 114 (E00D08). doi:10.1029/2009JE003339.
Ehlmann, B.L., et al., 2010. Geologic setting of serpentine deposits on Mars. Geophys Res Lett 37 (L06201). doi:10.1029/2010GL042596.
Ehlmann, B.L., et al., 2011. Evidence for low-grade metamorphism, hydrothermal alteration, and diagenesis on Mars from phyllosilicate mineral assemblages. Clays Clay Miner. 59 (4), 359–377.
El-Maarry, M.R., et al., 2010. Crater floor polygons: desiccation patterns of ancient lakes on Mars? J. Geophys. Res. 115, E10006.
El-Maarry, M.R., et al., 2012. Desiccation mechanism for formation of giant polygons on earth and intermediate-sized polygons on Mars: results from a pre-fracture model. Earth Planet. Sci. Lett. 323, 19–26.
El-Maarry, M.R., et al., 2014. Potential desiccation cracks on Mars: a synthesis from modeling, analogue-field studies, and global observations. Icarus 2014.
Farrow, C.E.G., Watkinson, D.H., 1992. Alteration and the role of fluids in Ni, Cu and platinum-group element deposition, Sudbury igneous complex contact, Onaping-Levack area. Ontario Mineral. Petrol. 46, 611–619.
Floerke, O.W., et al., 1991. Nomenclature of micro- and non-crystalline silica minerals, based on structure and microstructure. Neues. Jahrb. Min. Abh. 163, 19–42.
Goudge, T.A., et al., 2015. Assessing the mineralogy of the watershed and fan deposits of the Jezero crater paleolake system, Mars. J. Geophys. Res. Planets 120, 775–808. doi:10.1002/2014JE004782.
Hagerty, J.J., Newson, H.E., 2003. Hydrothermal alteration at the Lonar lake impact structure, India: implications for impact cratering on Mars. Meteorit. Planet. Sci. 38 (3), 365–381.
Hedenquist, J.W., 1987. Mineralization associated with volcanic-related hydrothermal systems in the circum-pacific basin. In: Transactions of the Fourth Circum–Pacific Energy and Mineral Resources Conference. Singapore, AAPG, pp. 513–524.
Ishibashi, J., Urabe, T., 1995. Hydrothermal Activity Related to Arc-Backarc Magmatism in the Western Pacific. Springer US, Backarc Basins, pp. 451–495.
Loizeau, D., et al., 2007. Phyllosilicates in the Mawrth Vallis region of Mars. J. Geophys. Res. 112 (E08S08). doi:10.1029/2006JE002877.
Loizeau, D., et al., 2012. Characterization of hydrated silicate-bearing outcrops in tyrrhena Terra, Mars: implications to the alteration history of Mars. Icarus 219, 476–497.
Malin, M.C., et al., 2007. Context camera investigation on board the Mars reconnaissance orbiter. J. Geophys. Res. 112, E05S04. doi:10.1029/2006JE002808.
Mangold, N., et al., 2012. Hydrothermal alteration in a late hesperian impact crater on Mars. In: 43th Lunar and Planetary Science. #1209.
Marzo, G.A., et al., 2010. Evidence for hesperian impact-induced hydrothermalism on Mars. Icarus 208, 667–683.
McEwen, A.S., et al., 2007. Mars reconnaissance orbiter's high resolution imaging science experiment (HiRISE). J. Geophys. Res. 112, E05S02.
McKeown, N.K., et al., 2009. Characterization of phyllosilicates observed in the central Mawrth Vallis region, Mars, their potential formational processes, and implications for past climate. J. Geophys. Res. 114, E00D10. doi:10.1029/2008JE003301.
McGuire, P.C., et al., 2009. An improvement to the volcano-scan algorithm for atmospheric correction of CRISM and OMEGA spectral data. Planet. Space Sci 57, 809–815.
Michalski, J.R., Niles, P.B., 2010. Deep crustal carbonate rocks exposed by meteor impact on Mars. Nat. Geosci. 3, 751–755.
Milliken, R.E., et al., 2008. Opaline silica in young deposits on Mars. Geology 36 (11), 847–850.
Moratto, S.Z.M., et al., 2010. Ames stereo pipeline, NASA's open source automated stereogrammetry. In: 41th LPSC. #2364.
Murchie, S., et al., 2007. Compact reconnaissance imaging spectrometer for Mars (CRISM) on Mars reconnaissance orbiter (MRO). J. Geophys. Res. 112, E05S03.
Mustard, J.F., et al., 2007. Mineralogy of the Nili fossae region with OMEGA/Mars express data: 1. Ancient impact melt in the Isidis basin and implications for the transition from the Noachian to Hesperian. J. Geophys. Res. 112 (E08S03).

Mustard, J.F., et al., 2008. Hydrated silicate minerals on Mars observed by the Mars reconnaissance orbiter CRISM instrument,. Nature 454, 305–309.
Naumov, M.V., 2005. Principal features of impact-generated hydrothermal circulation systems: mineralogical and geochemical evidence. Geofluids 5, 165–184.
Neubeck, A., et al., 2014. Olivine alteration and H2 production in carbonate-rich, low temperature aqueous environments. Planet. Space Sci 96, 51–61.
Neukum, G., et al., 2004. HRSC: The High Resolution Stereo Camera of Mars Express. ESA Special Publications SP-1240.
Newsom, H.E., 1980. Hydrothermal alteration of impact melt sheets with implications for Mars. Icarus 44, 207–216.
Noe Dobrea, E.Z., et al., 2010. Mineralogy and stratigraphy of phyllosilicate bearing and dark mantling units in the greater Mawrth Vallis west Arabia Terra area constraints on geological origin. J. Geophys. Res. 115 (E00D19). doi:10.1029/2009JE003351.
Osinski, G.R., et al., 2005a. A case study of impact-induced hydrothermal activity: the haughton impact structure, Devon Island, Canadian high arctic. Meteorit. Planet. Sci. 40 (12), 1859–1877.
Osinski, G.R., et al., 2005b. Hydrothermal activity associated with the ries impact event, Germany. Geofluids 5, 202–220.
Osinski, G.R., Pierazzo, E., 2013. Impact Cratering: Processes and Products. Wiley-Blackwell, p. 330. published by.
Osinski, G.R., et al., 2013. Impact-generated hydrothermal systems on Earth and Mars. Icarus doi:10.1016/j.icarus.2012.08.030.
Pan, L., Ehlmann, B.L., 2013. Phyllosilicate and hydrated silica detection in the Knobby terrains of acidalia planitia. In: 44th LPSC. #2572.
Parente, M., 2008. A new approach to denoising CRISM images. In: 39th LPSC. #2528.
Pelkey, S.M., et al., 2007. CRISM multispectral summary products: parameterizing mineral diversity on Mars from reflectance. J. Geophys. Res. 112 (E08S14). doi:10.1029/2006JE002831.
Pierazzo, E., et al., 2005. Starting conditions for hydrothermal systems underneath Martian craters: hydrocode modeling, large meteorite impacts. In: Kenkmann, T., Horz, F., Deutsch, A. (Eds.), Geol. Soc. Am. Spec. Paper, 384, pp. 443–457.
Pondrelli, M., et al., 2011. Mud volcanoes in the geologic record of Mars: the case of firsoff crater. Earth Planet. Sci. Lett. 304 (3-4), 511–519.
Poulet, F., et al., 2007. Martian surface mineralogy from observatoire pour la Mineralogie, l'Eau, les glaces et l'Activité on board the Mars express spacecraft (OMEGA/MEx): global mineral maps. J. Geophys. Res. 112 (E08S02). doi:10.1029/2006JE002840.
Rice, M.S., et al., 2013. Reflectance spectra diversity of silica-rich materials: sensitivity to environment and implications for detections on Mars. Icarus 223, 499–533.
Sapers, H.M., et al., 2012. The ries post-impact hydrothermal system spatial and temporal mineralogical variation. In: 43th LPSC. #1915.
Sapers, H.M., et al., 2015. Impact-generated hydrothermal activity beyond the ries crater rim. In: 46th LPSC. #2917.
Schade, U., et al., 2004. Near-infrared reflectance spectroscopy of Ca-rich clinopyroxenes and prospects for remote spectral characterization of planetary surfaces. Icarus 168, 80–92.
Schwenzer, S.P., Kring, D.A., 2013. Alteration minerals in impact-generated hydrothermal systems – Exploring host rock variability. Icarus 226, 487–496.
Schwenzer, S.P., Reed, M.H., 2013. Modeling alteration minerals on Mars - investigating the high temperature component. In: 44th LPSC. #2301.
Siebach, K.L., Grotzinger, J.P., 2014. Volumetric estimates of ancient water on mount sharp based on boxwork deposits, Gale Crater, Mars. J. Geophys. Res. Planets 119, 189–198. doi:10.1002/2013JE004508.
Skok, J.R., et al., 2010. Silica deposits in the Nili Patera caldera on the syrtis major volcanic complex on Mars. Nat. Geosci. 3, 838–841.
Skok, J.R., et al., 2012. A spectroscopic analysis of Martian crater central peaks: formation of the ancient crust. J. Geophys. Res. 117, E00J18. doi:10.1029/2012JE004148.
Smith, M.R., et al., 2013. Hydrated silica on Mars: combined analysis with near-infrared and thermal-infrared spectroscopy. Icarus 223 (2), 633–648.
Sunshine, J.M., et al., 2004. High-calcium pyroxene as an indicator of igneous differentiation in asteroids and meteorites. Meteorit. Planet. Sci. 39 (8), 1343–1357.
Tornabene, L.L., et al., 2009. Parautochthonous megabreccias and possible evidence of impact-induced hydrothermal alteration in holden crater, Mars. In: 40th LPSC. #1766.
Tornabene, L.L., et al., 2013. An impact origin for hydrated silicates on Mars: a synthesis. J. Geophys. Res. Planets 118, 994–1012.
Tornabene, L.L., et al., 2014. The pre-, syn- and post-impact origin of hydrated phases: a case study based on the remote sensing and ground-truth of the Haughton impact structure. In: Nunavut, Canada, 45th LPSC. #1777.
Viviano, C.E., et al., 2013. Implications for early hydrothermal environments on Mars through the spectral evidence for carbonation and chloritization reactions in the Nili fossae region. J. Geophys. Res. 118, 1858–1872.
Zurcher, L., Kring, D.A., 2004. Hydrothermal alteration in the Yaxcopoil-1 borehole, Chicxulub impact structure, Mexico. Meteorol. Planet. Sci. 39 (7), 1199–1222.
Wiseman, S.M., et al., 2013. Assessing variability among carbonate-bearing deposits on Mars. In: 44th LPSC. #2865.
Wray, J.J., et al., 2011. Evidence for regional deeply buried carbonate-bearing rocks on Mars. Lunar Planet. Sci. 42, 2635.
Wetherill, G.W., 1975. Late heavy bombardment of the moon and terrestrial planets. In: Lunar and Planetary Science Conference Proceedings, Vol. 6.